

Finding Quasars behind the Galactic Plane. IV. Candidate Selection from *Chandra* with Random Forest

XU ZHANG,¹ YANLI AI¹ , YANXIA ZHANG¹ , YUMING FU¹ , XUE-BING WU¹ , ZHIYING HUO¹ , WENFENG WEN,¹ JIAYUAN ZHOU,¹ DEXUAN KONG,¹ LINFENG ZENG,¹ AND HENG WANG¹

¹Shenzhen Key Laboratory of Ultraintense Laser and Advanced Material Technology, Center for Intense Laser Application Technology, and College of Engineering Physics, Shenzhen Technology University, Shenzhen 518118, People's Republic of China

²National Astronomical Observatories, Beijing 100101, People's Republic of China

³Leiden Observatory, Leiden University, Einsteinweg 55, 2333 CC Leiden, The Netherlands

⁴Kapteyn Astronomical Institute, University of Groningen, PO Box 800, 9700 AV Groningen, The Netherlands

⁵Department of Astronomy, School of Physics, Peking University, Beijing 100871, People's Republic of China

⁶Kavli Institute for Astronomy and Astrophysics, Peking University, Beijing 100871, People's Republic of China

ABSTRACT

Quasar samples remain severely incomplete at low Galactic latitudes because of strong extinction and source confusion. We conduct a systematic search for quasars behind the Galactic plane using X-ray sources from the *Chandra* Source Catalog (CSC 2.1), combined with optical data from *Gaia* DR3 and mid-infrared data from CatWISE2020. Using spectroscopically confirmed quasars and stars from data sets including DESI, SDSS, and LAMOST, we apply a Random Forest classifier to identify quasar candidates, with stellar contaminants suppressed using *Gaia* proper-motion constraints. Photometric redshifts are estimated for the candidates using a Random Forest regression model. Applying this framework to previously unclassified CSC sources, we identify 6286 quasar candidates, including 863 Galactic Plane Quasar (GPQ) candidates at $|b| < 20^\circ$, of which 514 are high-confidence candidates. Relative to the previously known GPQ sample, our selected GPQs reach fainter optical and X-ray fluxes, improving sensitivity to low-flux GPQs. In addition, both the GPQ candidates and known GPQs display harder X-ray spectra than the all-sky quasar sample, consistent with increased absorption through the Galactic plane. Pilot spectroscopy confirms two high-confidence GPQ candidates as quasars at spectroscopic redshifts of $z = 1.2582$ and $z = 1.1313$, and further spectroscopic follow-up of the GPQ sample is underway. This work substantially improves the census of GPQs and provides a valuable target sample for future spectroscopic follow-up, enabling the use of GPQs to refine the reference frames for astrometry and probe the Milky Way interstellar and circumgalactic media with the absorption features of GPQs.

1. INTRODUCTION

Quasars are among the most luminous active galactic nuclei (AGNs), powered by accretion onto supermassive black holes, and are detectable out to cosmological distances. Their high luminosities, compactness, and long-lived activity phases make quasars uniquely valuable probes for a wide range of astrophysical and cosmological questions, including the growth of supermassive black holes and their coevolution with host galaxies (e.g., T. Di Matteo et al. 2005; J. Kormendy & L. C. Ho 2013; X.-B. Wu et al. 2015; E. Bañados et al. 2018; K. Inayoshi et al. 2020; X. Fan et al. 2023), and the large-scale structure of the Universe through quasar clustering and baryon acoustic oscillations (e.g., D. J. Eisenstein

et al. 2005; K. S. Dawson et al. 2013; M. R. Blanton et al. 2017). In addition, quasars have negligible parallaxes and proper motions, making them ideal reference objects for defining and maintaining celestial reference frames (CRFs; e.g., C. Ma et al. 2009; Gaia Collaboration et al. 2022, 2023a). Despite major progress in wide-area surveys, however, the completeness of quasar samples remains poor close to the Galactic plane.

Over the past decades, major spectroscopic surveys have dramatically expanded the known quasar population. The Sloan Digital Sky Survey (SDSS; A. Almeida et al. 2023; D. G. York et al. 2000) and its extensions established the first homogeneous, large-area quasar samples (R. Soria & A. K. H. Kong 2002; D. P. Schneider et al. 2010; I. Páris et al. 2017; B. W. Lyke et al. 2020), while complementary efforts such as the 2dF QSO Redshift Survey and the LAMOST quasar survey extended quasar identification to different depths and sky regions

(S. M. Croom et al. 2004, 2009; Y. L. Ai et al. 2016; J.-J. Jin et al. 2023; B. Lyu et al. 2025). More recently, the Dark Energy Spectroscopic Instrument (DESI; DESI Collaboration et al. 2025) has delivered the largest spectroscopic quasar samples to date, with more than one million confirmed quasars now available for statistical studies. Despite this rapid progress, the sky distribution of known quasars remains highly non-uniform.

In particular, the census of quasars at low Galactic latitudes remains severely incomplete. Most optical and near-infrared surveys avoid regions close to the Galactic plane, where strong interstellar extinction, high stellar densities, and severe source confusion substantially degrade the effectiveness of traditional color-based selection techniques (D. J. Schlegel et al. 1998; N. P. Ross et al. 2012; G. T. Richards et al. 2002). As a consequence, the surface density of spectroscopically confirmed quasars decreases sharply toward the Galactic plane, producing a persistent gap in all-sky quasar samples (Y. Fu et al. 2021; Z.-Y. Huo et al. 2025). This incompleteness limits the use of quasars as uniform tracers of large-scale structure and as astrometric reference objects, and motivates dedicated searches for quasars in the low-latitude sky.

Quasars behind the Galactic plane (GPQs; $|b| \lesssim 20^\circ$), are nevertheless of considerable scientific importance. As distant extragalactic point sources with negligible parallaxes and proper motions, GPQs provide stable reference objects that are essential for constructing and validating celestial reference frames in the Galactic disk, where background sources are currently sparse (Gaia Collaboration et al. 2018a,b, 2023b). GPQs also serve as bright background beacons for absorption-line studies of the Milky Way interstellar and circumgalactic media, enabling measurements of gas kinematics, dust extinction, and chemical abundances along heavily obscured sightlines that are under-sampled at high Galactic latitudes (e.g., B. D. Savage & K. R. Sembach 1996; P. Richter 2006; Y. Fu et al. 2021, 2024).

Identifying GPQs is observationally challenging. The Galactic plane hosts a dense and diverse population of stars, binaries, and other Galactic sources, including many X-ray emitters, and these contaminants can overlap quasars in color–color and color–magnitude spaces. As a result, GPQs have been explored in relatively few dedicated studies. Early efforts by M. Im et al. (2007) uncovered dozens of bright QSOs/AGNs at $|b| < 20^\circ$ using radio and near-infrared criteria. A major advance was achieved by Y. Fu et al. (2021), who applied transfer learning to optical and infrared data from Pan-STARRS1 (PS1; K. C. Chambers et al. 2016) DR1 and AllWISE (E. L. Wright et al. 2010; R. M. Cutri

et al. 2013), producing a catalog of roughly 160,000 GPQ candidates within $|b| < 20^\circ$. Subsequent follow-up spectroscopy confirmed approximately 200 GPQs with high success rates (Y. Fu et al. 2022). J. Werk et al. (2024) later confirmed 72 UV-bright AGNs at $|b| < 30^\circ$, with 25 newly recognized objects, and the LAMOST GPQ program has recently reported ~ 1300 additional GPQs based on LAMOST DR10 (Z.-Y. Huo et al. 2025). These studies demonstrate that combining multiwavelength data with modern classification approaches is essential for making progress in the Galactic plane.

Machine-learning methods applied to multi-band photometry and astrometry can exploit high-dimensional information to improve quasar selection in crowded fields (G. T. Richards et al. 2002; D. Carrasco et al. 2015; Gaia Collaboration et al. 2023a; Y. Fu et al. 2025). X-ray observations provide a powerful and complementary avenue for identifying quasars with extreme properties (H. Wang et al. 2025) or X-ray sources in the Galactic disk (T. Bao et al. 2025). Among current X-ray facilities, the *Chandra* X-ray Observatory is uniquely advantageous for low-latitude work: its sub-arcsecond angular resolution substantially mitigates source confusion in dense stellar regions, enabling more reliable associations between X-ray sources and their optical/infrared counterparts. The *Chandra* Source Catalog (CSC; here we use CSC 2.1) therefore offers an excellent basis for constructing GPQ candidates, provided that Galactic X-ray source contamination can be effectively controlled.

In this work, we present the fourth paper in the “Finding Quasars behind the Galactic Plane” series, focusing on GPQ candidate selection using CSC 2.1 and a Random Forest (RF) classifier. We cross-match CSC sources with *Gaia* DR3 and CatWISE2020 to assemble optical, mid-infrared, and X-ray features for classification. To reduce contamination from extended sources and problematic photometry in crowded regions, we apply quality screening based on the *Gaia* corrected BP/RP flux excess factor (C^*). We build a spectroscopically confirmed training set by cross-matching with DESI, SDSS, and LAMOST catalogs, train an RF classifier to identify quasar candidates, and then incorporate *Gaia* proper motions to further suppress stellar contaminants. We also estimate photometric redshifts for the quasar candidates using an RF regressor. The resulting catalog contains 6286 quasar candidates in total, including 863 GPQ candidates, with a substantial high-confidence subset. Finally, we report initial spectroscopic confirmation of two GPQ candidates, as part of an ongoing follow-up program.

This paper is organized as follows. In Section 2, we describe the CSC 2.1 data and the multi-wavelength pho-

tometric and astrometric information used in this work, as well as the construction of the training sample. Section 3 introduces the RF classification framework, the adopted features, and the performance of the classifier. In Section 4, we present the RF-based photometric redshift estimation for the quasar candidates. The classification results and the properties of the selected GPQ candidates are discussed in Section 5. Finally, we summarize our main results and conclusions in Section 6. We adopt a flat universe with $\Omega_M = 0.3$ and $\Omega_\Lambda = 0.7$, and a cosmological parameter $H_0 = 70 \text{ km s}^{-1} \text{ Mpc}^{-1}$.

2. DATA

2.1. CSC2.1 and Multi-Wavelength Data

We used *Chandra* Source Catalog version 2.1 (CSC 2.1; I. N. Evans et al. 2024) Master Sources Table to select GPQ candidates. It includes measured properties for 407,806 unique compact and extended X-ray sources and more than 1.3 million individual detections observed with either ACIS or HRC-I observations released publicly before the end of 2021. Most of these sources remain unidentified. *Chandra* has two focal plane instruments: Advanced CCD Imaging Spectrometer (ACIS) and High Resolution Camera (HRC). The ACIS instrument observes in broad (b): 0.5–7.0 keV, ultrasoft (u): 0.2–0.5 keV, soft (s): 0.5–1.2 keV, medium (m): 1.2–2.0 keV, and hard(h): 2.0–7.0 keV bands. The HRC instrument observes in 0.1–10 keV energy band and is designated as ‘W’ band. The energy flux in each band is determined using aperture photometry. The source count is derived from an elliptical source region and subtracted by the background count in the surrounding region. To convert the count rate to energy flux, the total count rate is summed up and then scaled by the local ancillary response function.

In this work, we use aperture-corrected average net-flux in b, u, s, m, and h bands, which are named as *b-csc*, *u-csc*, *s-csc*, *m-csc*, *h-csc*, respectively. We applied several constraints to the CSC 2.1 data to ensure quality. First, we selected only point sources with the extent flag set to 0 in the catalog. We then applied additional filters based on the following CSC 2.1 quality flags: *pileup_flag*, *sat_src_flag*, *conf_flag*, *streak_src_flag* (Table 1). Through this process, a total of 364,555 unique high-quality X-ray point sources were selected from CSC 2.1.

We then cross-match these 364,555 unique CSC 2.1 sources with the CatWISE2020 (P. R. M. Eisenhardt et al. 2020) and *Gaia* DR3 catalogues to obtain their multi-wavelength properties. A matching radius of $3''$ is adopted for CatWISE2020 and $1''.5$ for *Gaia* DR3, us-

ing the TOPCAT⁷ software (M. B. Taylor 2005) for the cross-matching. For the CatWISE2020 counterparts, we apply filters to retain sources with magnitudes in the ranges $8 < W1 < 17.7$ and $7 < W2 < 17.5$, and corresponding magnitude errors $\sigma \leq 0.2$, ensuring that the magnitudes are below the nominal limiting magnitudes in each band. For the *Gaia* DR3 counterparts, we require $G < 21$ mag and a photometric error less than 0.2. All *Gaia* magnitudes are then corrected for extinction using the two-dimensional dust reddening map from Planck Collaboration et al. (2016). To mitigate the potential impact of bright sources on classification performance, we further exclude objects with extinction-corrected *G*-band magnitudes brighter than 10.

To improve the purity of the GPQ candidate sample, we then remove potential optically extended sources using the following procedure. We refine the point-source selection by applying the corrected BP/RP photometric excess factor, C^* , derived from *Gaia* DR3 (M. Riello et al. 2021), which provides an additional constraint on source morphology. The original BP/RP excess factor, C , is defined as the ratio of the summed BP and RP integrated fluxes to the *G*-band flux:

$$C = \frac{I_{\text{BP}} + I_{\text{RP}}}{I_G}. \quad (1)$$

Because the BP and RP photometric windows are broader than that of the *G* band, extended sources tend to exhibit systematically larger excess factors than point sources (e.g., C. Liu et al. 2020). The corrected excess factor C^* mitigates the color dependence inherent in C , providing a more reliable diagnostic of source extension (M. Riello et al. 2021). To compress the dynamic range and suppress the influence of extreme outliers, we impose the criterion $\log(1 + C^*) \leq 0.5$, which yields a cleaner point-source sample (e.g., Y. Fu et al. 2025). Finally 36,152 sources are selected with high-quality measurements from CSC 2.1, CatWISE2020, and *Gaia* DR3.

Table 1. Quality Flags Used to Filter Sources in CSC 2.1 and Their Description

Flag code	Description
extent_flag	Extended or non-point-like at 90% CL.
pileup_flag	ACIS pile-up fraction exceeds $\sim 10\%$
sat_src_flag	Saturated source in all observations
conf_flag	Source confused (source and/or background regions in different stacks may overlap)
streak_src_flag	Source on ACIS CCD readout streak

⁷ <https://www.star.bris.ac.uk/~mbt/topcat/>

Hereafter, we refer to this sample as the CSC–WISE–GAIA sample.

2.2. The Training Set

A well-defined and representative training set is critical for the supervised classification of quasars and stars, particularly in the crowded and heterogeneous environments near the Galactic plane. Following the construction of the CSC–WISE–GAIA sample described in Section 2.1, we compile spectroscopically confirmed quasar and stellar samples from multiple surveys and catalogs to serve as labeled data for training the RF classifier.

We first identify quasars by cross-matching the CSC–WISE–GAIA sample with spectroscopically confirmed quasars from DESI DR1 (DESI Collaboration et al. 2025) and SDSS DR18 (A. Almeida et al. 2023), adopting a matching radius of $1''$. To improve completeness, this initial quasar sample is further supplemented with confirmed quasars from the Million Quasars Catalog (E. W. Flesch 2023), the LAMOST spectroscopic surveys (X.-Q. Cui et al. 2012; A.-L. Luo et al. 2015), and the Galactic Plane quasar sample identified from LAMOST DR10 by Z.-Y. Huo et al. (2025). All supplementary quasar catalogs are cross-matched with the CSC–WISE–GAIA sample using a $3''$ radius to ensure consistent source associations.

For the stellar class, we similarly cross-match the CSC–WISE–GAIA sample with DESI DR1 and SDSS DR18 to identify spectroscopically classified stars. To better represent the diverse Galactic X-ray source population that may contaminate quasar selection, we further include several specialized stellar catalogs. These include Galactic Wolf–Rayet stars (K. A. van der Hucht 2001, 2006) and APOGEE-2 stars from SDSS DR16 (H. Jönsson et al. 2020); young stellar objects (YSOs) in open clusters and molecular clouds (e.g., H. Ozawa et al. 2005; G. Giardino et al. 2007; A. J. Delgado et al. 2011; M. S. Povich et al. 2011; L. M. Rebull et al. 2011; S. T. Megeath et al. 2012); high-mass X-ray binaries (HMXBs) and related Galactic and nearby extragalactic sources (Q. Z. Liu et al. 2006; R. Walter et al. 2015; S. Mineo et al. 2012; S. Sazonov & I. Khabibullin 2017); low-mass X-ray binaries (LMXBs) compiled from the Ritter–Kolb catalog and subsequent updates (H. Ritter & U. Kolb 2015; Q. Z. Liu et al. 2007; S. Sazonov et al. 2020; A. Kundu et al. 2007; P. J. Humphrey & D. A. Buote 2008; Z. Zhang et al. 2011); and cataclysmic variables (CVs) (R. A. Downes et al. 2001; H. Ritter & U. Kolb 2015). These catalogs are cross-matched with the CSC–WISE–GAIA sample using a matching radius of $3''$.

Table 2. The Number of Sources in the Training Set

Class	% of training set	No.
QSO	61.88	8489
STAR	38.12	5229
Total training set		13,718
Unidentified Sources		22,434
Total		36,152

Sources that are not matched to any of the above quasar or stellar catalogs are subsequently queried against the SIMBAD database (M. Wenger et al. 2000) within a $3''$ radius. Entries flagged as “NOT GOOD” are excluded. After applying these procedures, the final training set consists of 8489 quasars and 5229 stars, as summarized in Table 2. The remaining 22,434 sources in the CSC–WISE–GAIA sample lack reliable spectroscopic classifications and are treated as unlabeled objects for subsequent prediction.

Although the training set is not strictly balanced, it provides broad coverage of photometric, astrometric, and X-ray parameter space for both quasars and stars. This construction is designed to reduce overfitting and to enable the RF classifier described in Section 3 to robustly distinguish quasars from stellar contaminants in the low-latitude sky.

3. METHOD

3.1. Random Forest Classification

We employ a RF classifier to distinguish quasars from stars in the CSC–WISE–GAIA sample. RF is an ensemble learning algorithm based on decision trees and bootstrap aggregation, originally introduced by T. K. Ho (1995) and later formalized by L. Breiman (2001). By combining multiple weak learners trained on bootstrapped subsets of the data and randomly selecting input features at each split, the RF algorithm effectively mitigates overfitting and performs robustly in high-dimensional parameter space.

The RF classifier is implemented using the `scikit-learn`⁸ machine-learning library (F. Pedregosa et al. 2011). Each decision tree is trained independently, and the final classification is determined by a majority vote across all trees. For each source, the fraction of trees voting for the quasar class is interpreted as the quasar membership probability, providing a quantitative measure of classification confidence.

To separate quasars from stars, we adopt a total of 31 input features that incorporate multi-wavelength pho-

⁸ <https://scikit-learn.org/stable/index.html>

tometric, astrometric, and X-ray information. These features include X-ray fluxes and hardness ratios from CSC 2.1, optical and mid-infrared magnitudes and colors from *Gaia* DR3 and WISE, extinction-related quantities, and astrometric parameters such as proper motion and parallax significance. A complete list and description of the adopted features are provided in Table 3.

Missing values may arise from limited survey depth, nondetections, or incomplete coverage in specific bands. To allow uniform processing of incomplete data, all missing entries are assigned a sentinel value of -9999 , enabling the RF algorithm to handle such cases consistently during training and prediction.

The RF model includes several tunable hyperparameters, whose optimization is critical for achieving optimal classification performance. We focus on three key parameters: the number of trees in the ensemble ($n_{\text{estimators}}$), the number of features considered at each split ($\text{max}_{\text{features}}$), and the maximum depth of individual trees ($\text{max}_{\text{depth}}$). These hyperparameters are optimized using a grid search with five-fold cross-validation. The optimal configuration yields $\text{max}_{\text{features}} = \log_2 31$ and $n_{\text{estimators}} = 41$, while no explicit upper limit on $\text{max}_{\text{depth}}$ is required based on the validation results.

After hyperparameter optimization, the labeled dataset is randomly divided into a training subset and an independent validation subset with a ratio of 4:1. The RF classifier is trained on the training subset and evaluated on the validation subset. Classification performance is assessed using standard metrics for binary classification, including accuracy, precision, recall, and the $F1$ -score, defined as

$$\text{Accuracy} = \frac{\text{TP} + \text{TN}}{\text{TP} + \text{TN} + \text{FP} + \text{FN}}, \quad (2)$$

$$\text{Precision} = \frac{\text{TP}}{\text{TP} + \text{FP}}, \quad (3)$$

$$\text{Recall} = \frac{\text{TP}}{\text{TP} + \text{FN}}, \quad (4)$$

$$F1 = 2 \times \frac{\text{Precision} \times \text{Recall}}{\text{Precision} + \text{Recall}}, \quad (5)$$

where TP, TN, FP, and FN denote true positives, true negatives, false positives, and false negatives, respectively.

The normalized confusion matrix for the binary classification task, evaluated on the validation set and shown in Figure 1, demonstrates the strong performance of the trained RF classifier. The model correctly classifies 99.44% of quasars and 98.50% of stars, with minimal contamination between the two classes. This performance

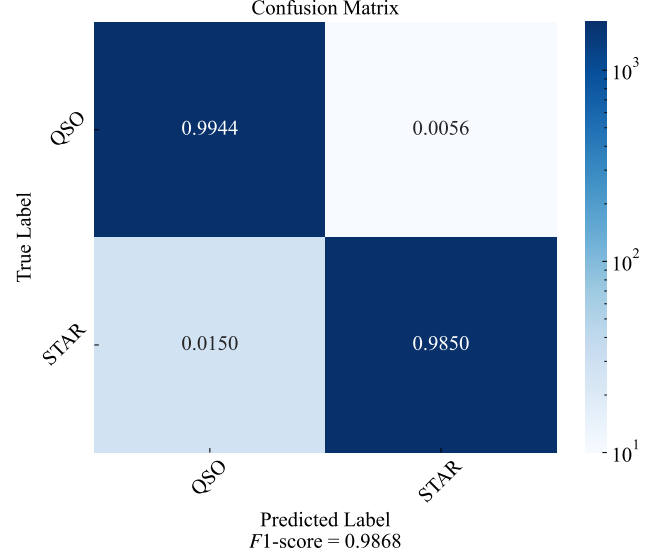


Figure 1. Normalized confusion matrix of the RF classifier computed on the validation set. The matrix is color-coded by the number of sources in each cell. Diagonal entries show the fraction of correctly classified objects (i.e., recall or completeness) for each class, while off-diagonal entries indicate the misclassification rates.

is further supported by an overall $F1$ -score of 0.9868, indicating consistently high precision and recall.

4. REDSHIFT ESTIMATION FOR QUASAR CANDIDATES

We estimate photometric redshifts for the quasar candidates identified by the RF classifier using an RF-based regression model. Reliable redshift estimation is essential for characterizing the statistical properties of the candidate sample and for enabling subsequent population studies, particularly in regions where spectroscopic follow-up is incomplete.

The RF regression model is trained using spectroscopically confirmed quasars from the training set described in Section 2.2. To evaluate the performance of the regression, we adopt two commonly used metrics: the root mean square error (RMSE) and the coefficient of determination (R^2), defined as

$$\text{RMSE} = \sqrt{\frac{1}{n} \sum_{i=1}^n (z_i - \hat{z}_i)^2}, \quad (6)$$

$$R^2 = 1 - \frac{\sum_{i=1}^n (z_i - \hat{z}_i)^2}{\sum_{i=1}^n (z_i - \bar{z})^2}, \quad (7)$$

where z_i and \hat{z}_i are the spectroscopic and predicted redshifts of the i th source, respectively, \bar{z} is the mean spectroscopic redshift of the sample, and n is the total number of sources. The RMSE quantifies the typical deviation between predicted and true redshifts, while R^2

Table 3. Features in This Work

Feature	Feature description
gal_l	Galactic Longitude
gal_b	Galactic Latitude
b-csc	Flux in ACIS broad (<i>b</i>) band (0.5–7.0 keV)
s-csc	Flux in ACIS soft (<i>s</i>) band (0.5–1.2 keV)
m-csc	Flux in ACIS medium (<i>m</i>) band (1.2–2.0 keV)
h-csc	Flux in ACIS hard (<i>h</i>) band (2.0–7.0 keV)
HR _{hm}	ACIS hard (2.0–7.0 keV) - medium (1.2–2.0 keV) energy band hardness ratio
HR _{hs}	ACIS hard (2.0–7.0 keV) - soft (0.5–1.2 keV) energy band hardness ratio
HR _{ms}	ACIS medium (1.2–2.0 keV) - soft (0.5–1.2 keV) energy band hardness ratio
nh_gal	Galactic N_H column density in direction of source
log(f_x)	logarithm of X-ray flux in 0.5–7 keV (<i>b</i> band)
log(f_x/f_g)	logarithm of X-ray-to-optical flux ratio
<i>G</i>	<i>Gaia</i> DR3 <i>G</i> -band magnitude
<i>BP</i>	<i>Gaia</i> DR3 <i>BP</i> -band magnitude
<i>RP</i>	<i>Gaia</i> DR3 <i>RP</i> -band magnitude
W1	WISE W1 band magnitude
W2	WISE W2 band magnitude
A_V	Interstellar Extinction
log(f_g)	logarithm of <i>G</i> band flux
log(f_{BP})	logarithm of <i>BP</i> band flux
log(f_{RP})	logarithm of <i>RP</i> band flux
PM	Total proper motion
PLXSIG	parallax significance defined as $ \frac{\text{PARALLAX}}{\text{PARALLAX_ERROR}} $
PMSIG	proper motion significance defined as $\sqrt{\left(\frac{\text{PMRA}}{\text{PMRA_ERROR}}\right)^2 + \left(\frac{\text{PMDEC}}{\text{PMDEC_ERROR}}\right)^2}$
<i>BP</i> – <i>RP</i>	<i>BP</i> – <i>RP</i> color
<i>BP</i> – <i>G</i>	<i>BP</i> – <i>G</i> color
<i>G</i> – <i>RP</i>	<i>G</i> – <i>RP</i> color
<i>RP</i> – W1	<i>RP</i> – W1 color
<i>G</i> – W1	<i>G</i> – W1 color
<i>G</i> – W2	<i>G</i> – W2 color
W1 – W2	W1 – W2 color

measures the fraction of variance in the spectroscopic redshifts explained by the regression model.

Photometric redshift estimation based solely on *Gaia* photometry is limited by the broad optical passbands and the lack of detailed spectral information. To improve regression performance, we incorporate additional optical photometry from the Pan-STARRS1 (PS1; [K. C. Chambers et al. 2016](#)) survey, which provides five broad-band filters (*g*, *r*, *i*, *z*, and *y*). For sources not covered by PS1, photometry from the NOIRLab Source Catalog DR2 (NSC DR2; [D. L. Nidever et al. 2021](#)) is adopted as a substitute. These data enable the construction of more informative color indices that better trace redshift-dependent spectral features.

In total, we adopt 18 input features for the RF regression model. These include the optical, infrared,

and astrometric color indices $g - r$, $r - i$, $i - z$, $z - y$, z -W1, y -W1, W1-W2, $G_{\text{BP}} - G_{\text{RP}}$, $G_{\text{BP}} - G$, $G - G_{\text{RP}}$, $G_{\text{RP}}\text{-W1}$, $G\text{-W1}$, and $G\text{-W2}$, as well as $\log(f_x)$, $\log(f_x/f_g)$, $\log(1 + C^*)$, $\log(1 + z_{\text{low}})$, and $\log(1 + z_{\text{up}})$. Here, z_{low} (`redshift_qsoc_lower`) and z_{up} (`redshift_qsoc_upper`) correspond to the 0.15866 and 0.84134 quantiles of the *Gaia*-based redshift estimate z_{Gaia} , representing the lower and upper confidence bounds, respectively.

The trained RF regression model is applied to all quasar candidates to derive photometric redshift estimates. Figure 2 shows the resulting redshift distributions for the all-sky quasar candidate sample and for the subset of GPQ candidates. The redshift distribution of the GPQs is broadly consistent with that of the all-sky sample, indicating that the RF regression

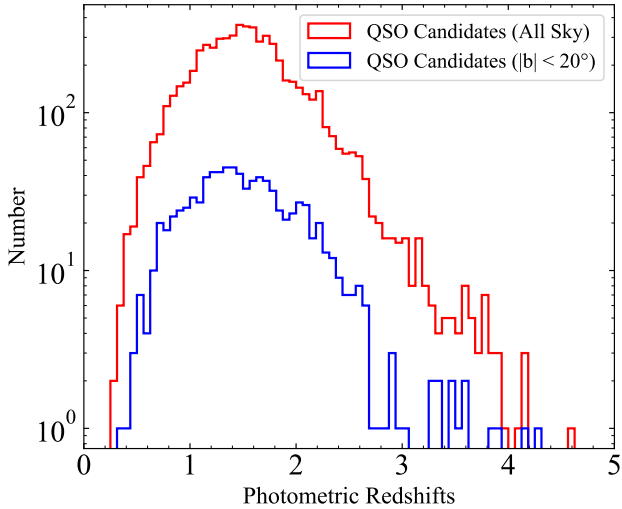


Figure 2. Distribution of RF-based photometric redshifts for the quasar candidates. The red histogram shows the full-sky candidate sample, and the blue histogram shows candidates at low Galactic latitude ($|b| < 20^\circ$). The ordinate shows source counts (logarithmic scale).

model does not introduce significant redshift-dependent biases in the low-latitude regime. These photometric redshifts provide a useful statistical characterization of the quasar candidate population and serve as a basis for future spectroscopic follow-up observations.

5. RESULTS

5.1. Classification Results

We apply the trained RF classifier to the 22,434 previously unclassified sources in the CSC–WISE–GAIA sample, i.e., sources without reliable spectroscopic classifications. Of these, 7723 sources are classified as quasar candidates and 14,711 as stars. Figure 3 presents the distribution of the resulting quasar and stellar candidates in the G versus $W1 - W2$ color–magnitude diagram.

Among the previously unclassified sources, 11,751 are located within the Galactic plane ($|b| < 20^\circ$). Of these, 1110 sources (9.45%) are classified as quasar candidates, while the remaining 10,641 sources are classified as stars, reflecting the strong dominance of Galactic stellar populations at low Galactic latitudes.

To further suppress stellar contamination, we apply an additional selection based on *Gaia* proper motions. We adopt the probabilistic zero–proper-motion criterion introduced by Y. Fu et al. (2021, 2024, 2025), which explicitly accounts for measurement uncertainties. The probability density of zero proper motion, f_{PM0} , is defined as

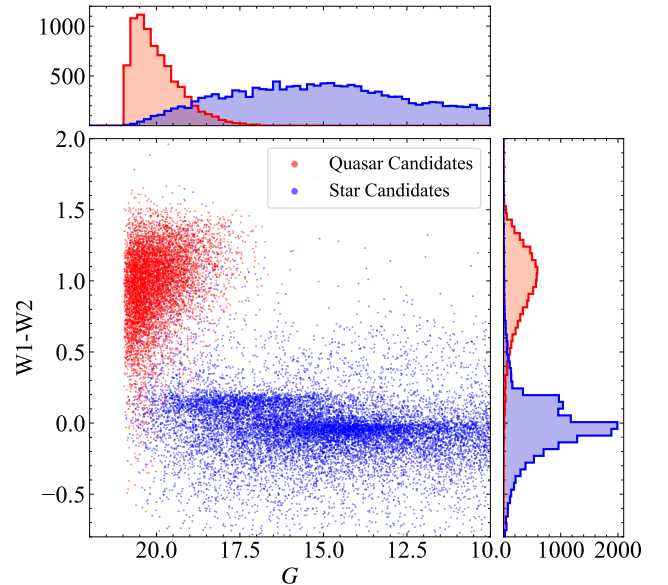


Figure 3. Distribution of the all-sky candidates in the G versus $W1 - W2$ diagram as classified by the RF model. Red and blue points denote quasar and stellar candidates, respectively; the top and right panels show the corresponding marginal distributions in G and $W1 - W2$. The G magnitudes shown on the horizontal axis are corrected for Galactic extinction. We apply a uniform magnitude filter to all candidates, excluding sources with observed $G > 21$ mag (prior to extinction correction) and removing very bright objects with $G < 10$ mag.

$$f_{PM0} = \frac{1}{2\pi\sigma_x\sigma_y\sqrt{1-\rho^2}} \times \exp\left[-\frac{1}{2(1-\rho^2)}\left(\frac{x^2}{\sigma_x^2} - \frac{2\rho xy}{\sigma_x\sigma_y} + \frac{y^2}{\sigma_y^2}\right)\right], \quad (8)$$

where x is the proper motion in R.A. (`pmra`), y is the proper motion in Decl. (`pmdec`), σ_x and σ_y are the corresponding uncertainties, and ρ is the correlation coefficient between x and y (`pmra_pmdec_corr`). For a given uncertainty level, sources with smaller proper motions yield higher values of f_{PM0} by construction.

Figure 4 shows the distributions of $\log(f_{PM0})$ for spectroscopically confirmed quasars, spectroscopically confirmed stars, and the quasar candidates. We adopt a conservative threshold of $\log(f_{PM0}) \geq -4$, which efficiently removes stellar contaminants while retaining the majority of quasars. Applying this criterion excludes 1437 sources initially classified as quasar candidates.

After the proper-motion filtering, the final quasar candidate sample contains 6286 sources across the entire sky. Among these, 863 sources are located behind the Galactic plane ($|b| < 20^\circ$) and are identified as GPQ candidates. Of the GPQs, 514 sources have quasar mem-

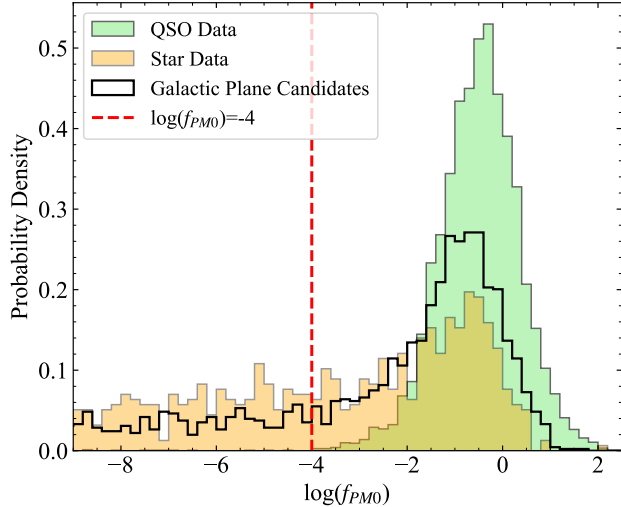


Figure 4. Distributions of $\log(f_{PM0})$, the probability density at zero proper motion derived from *Gaia* astrometry (see Eq. 8), for spectroscopically confirmed quasars (green), spectroscopically confirmed stars (yellow), and the GPQ candidates (white). The vertical dashed line marks the adopted threshold $\log(f_{PM0}) = -4$ used to suppress stellar contaminants; note that f_{PM0} is a probability density (not a probability) and therefore can exceed unity.

bership probabilities greater than 0.8 and are therefore considered high-confidence GPQ candidates. The spatial distribution of the GPQ candidates in Galactic coordinates is shown in Figure 5. A subset of these high-confidence GPQ candidates is presented in Table 4. The whole selected GPQs and all-sky quasar candidates are available at <https://github.com/jeepsmoker288/GPQs-and-all-sky-quasar-candidates>.

5.2. Properties of GPQ Candidates

The GPQ candidates identified in this work exhibit distinct X-ray and multi-wavelength properties compared with the all-sky quasar candidate sample. In particular, GPQs show systematically harder X-ray spectra. Figure 6 compares the distributions of the hard-soft energy band hardness ratio (HR_{hs}) for quasars in the spectroscopic training set and for the quasar candidates, separated into all-sky and low Galactic latitude ($|b| < 20^\circ$) subsamples. In both the training set and the candidate sample, sources located at $|b| < 20^\circ$ display higher hardness ratios than all-sky sources.

This systematic hardening is not indicative of intrinsic differences in quasar accretion properties, but instead reflects the effects of strong Galactic absorption along low-latitude sightlines. Soft X-ray photons are preferentially absorbed by interstellar gas and dust in the Galactic plane, whereas higher-energy photons are less affected. The close agreement between the hardness-

ratio distributions of the GPQ candidates and those of spectroscopically confirmed GPQs in the training set indicates that the RF classifier effectively captures this absorption-driven spectral signature.

Figure 7 compares the distributions of optical (G), mid-infrared (W1), and X-ray fluxes, as well as redshift (spectroscopic or RF-based photometric redshift), between the training-set quasars and the GPQ candidates. In all wavelength regimes, the GPQ candidates are systematically fainter than the quasars in the training set. The G and W1 magnitude distributions are shifted toward fainter values, and the X-ray flux distribution peaks at lower fluxes.

These trends indicate that the present selection method is sensitive to quasars that lie beyond the effective depth of existing spectroscopic samples. The fainter optical and infrared magnitudes of the GPQ candidates are consistent with significant dust extinction in the Galactic plane, while their lower X-ray fluxes suggest that this work probes a previously underexplored population of faint or heavily obscured quasars behind the Galactic disk.

We further compare the GPQ candidates identified in this work with the unified all-sky quasar candidate catalog CatGlobe (Y. Fu et al. 2025). Of the 863 GPQ candidates, 617 have counterparts in CatGlobe, while 246 do not. The unmatched candidates show no significant differences from the matched subset in their color-magnitude distributions, X-ray fluxes, or redshift distributions, indicating that they likely belong to the same underlying quasar population. The presence of these additional candidates highlights the importance of incorporating X-ray information in quasar selection, particularly for uncovering quasars missed by purely optical and infrared approaches in the heavily obscured regions of the Galactic plane.

5.3. Spectroscopic Follow-up of GPQ Candidates

The most critical next step is spectroscopic confirmation of the candidate GPQs. This will definitively validate the RF method’s accuracy, measure precise redshifts, and allow for detailed studies of the physical properties (e.g., black hole masses, accretion rates) of these previously hidden quasars. To provide an initial validation of our GPQ candidate selection, we obtained pilot optical spectroscopy for two high-confidence GPQ candidates, 2CXO J031404.4+403900 and 2CXO J031712.7+405301. The observations were carried out on 2025 December 14 (UT) with the Palomar 200-inch (P200) Hale telescope using the Next Generation Palomar Spectrograph (NGPS; H. Jiang et al. 2018). NGPS records simultaneous spectra in two chan-

Table 4. Selected GPQ Candidates by the RF Classifier. An excerpt of the GPQ candidate catalog is shown for guidance. The full machine-readable table is available at <https://github.com/jeepsmoker288/GPQs-and-all-sky-quasar-candidates>.

Name	R.A.	Decl.	W1	W2	G	$\log(f_x)$	P_{QSO}	z_{phot}
2CXO J011808.4+453857	19.5354	45.6492	15.244	14.510	20.2034	-13.5972	0.9756	1.1070
2CXO J022142.3+421947	35.4264	42.3297	16.116	15.646	20.0635	-14.1680	0.9756	3.4535
2CXO J031404.4+403900	48.5184	40.6500	15.697	14.590	19.3212	-13.1726	0.9024	1.1544
2CXO J031711.4+421654	49.2975	42.2819	16.092	15.515	20.5539	-13.7589	0.9512	1.1133
2CXO J031712.7+405301	49.3031	40.8838	14.768	13.349	19.2251	-12.7701	0.8537	0.7809
2CXO J040239.4+260839	60.6643	26.1442	16.309	15.383	20.3126	-13.6567	0.9512	1.2689
2CXO J061640.3-215410	94.1681	-21.9029	16.929	16.060	20.5411	-14.0410	0.9268	2.0291
2CXO J062659.7-352937	96.7488	-35.4936	15.620	14.678	20.3614	-13.8247	0.9024	1.6355
2CXO J075142.4-014522	117.9268	-1.7564	15.725	15.314	20.7567	-13.4226	0.9268	1.8400
2CXO J075255.9+122712	118.2330	12.4535	15.733	15.107	18.8968	-13.5895	1.0000	3.5815
2CXO J081813.4-073306	124.5558	-7.5520	16.557	16.032	20.0714	-13.7727	0.9268	1.7899
2CXO J082705.8-070859	126.7744	-7.1499	15.624	15.286	20.1933	-14.1581	0.9024	3.2615
2CXO J082732.9-070831	126.8873	-7.1420	16.023	14.801	19.9085	-14.0502	0.9756	2.0211
2CXO J084138.9-173123	130.4121	-17.5232	16.396	15.849	20.6588	-14.0028	0.9024	1.6542
2CXO J100023.3-302411	150.0970	-30.4030	15.895	14.910	20.3972	-13.7827	0.9756	1.0419
2CXO J102512.1-472309	156.3008	-47.3860	15.727	14.932	20.3067	-13.4771	0.9756	0.9385
2CXO J104151.1-704759	160.4631	-70.7999	15.621	14.776	20.1958	-13.2347	0.9756	1.2306

Note. All G band magnitudes have been corrected for Galactic dust extinction using [Planck Collaboration et al. \(2016\)](#) dust map. $\log(f_x)$ is the logarithm of X-ray flux in 0.5-7keV (b band). P_{QSO} is the classification probability of QSOs. z_{phot} is the photometric redshift.

nels, covering approximately 580–780 nm (R channel) and 760–1040 nm (I channel). We used a 1''.5 slit for both targets.

The NGPS data were reduced with the PYPEIT⁹ spectroscopic reduction pipeline ([J. Prochaska et al. 2020](#)), following standard long-slit procedures. Briefly, the two-dimensional frames were bias/overscan corrected and flat-fielded, after which the object trace was determined in each channel. Sky/background was estimated from source-free regions adjacent to the trace and subtracted, and one-dimensional spectra were extracted with a fixed-width aperture centered on the trace. Wavelength solutions were derived from arc-lamp exposures obtained in the standard NGPS calibration sequence. The R- and I-channel spectra were then placed on a consistent relative scale and combined by normalizing in their overlap region to produce a continuous spectrum for each target. Standard-star observations from the same run were used for relative flux calibration and to mitigate telluric absorption features.

In Figure 8 we present the spectra of the two identified GPQs. Redshifts were measured from identified broad emission lines, using multiple features where available. For 2CXO J031404.4+403900, we detect promi-

gent Mg II together with [O II] and [Ne III], as well as Balmer emission ($H\delta$, $H\gamma$, and $H\beta$), yielding $z = 1.2582$. For 2CXO J031712.7+405301, Mg II, [O II], and [Ne III] are detected along with Balmer emission, giving $z = 1.1313$. These confirmations provide a proof of concept that our X-ray plus multi-wavelength RF framework can recover genuine quasars behind the Galactic plane and motivate more extensive spectroscopic follow-up of the full GPQ candidate sample.

6. SUMMARY AND CONCLUSIONS

In this work, we present a systematic search for quasars located behind the Galactic plane using X-ray-selected sources from the *Chandra* Source Catalog (CSC 2.1), combined with optical and mid-infrared data from *Gaia* DR3 and CatWISE2020. By exploiting the high angular resolution of *Chandra* and the complementary diagnostic power of multi-wavelength information, we address the long-standing incompleteness of quasar samples at low Galactic latitudes.

We construct a high-quality CSC–WISE–GAIA sample through a series of photometric, astrometric, and morphological quality cuts designed to mitigate source confusion and contamination in crowded fields. Using spectroscopically confirmed quasars and stars compiled from DESI, SDSS, LAMOST, and the literature, we train a RF classifier to distinguish quasars from Galactic

⁹ <https://pypeit.readthedocs.io/en/release/index.html>

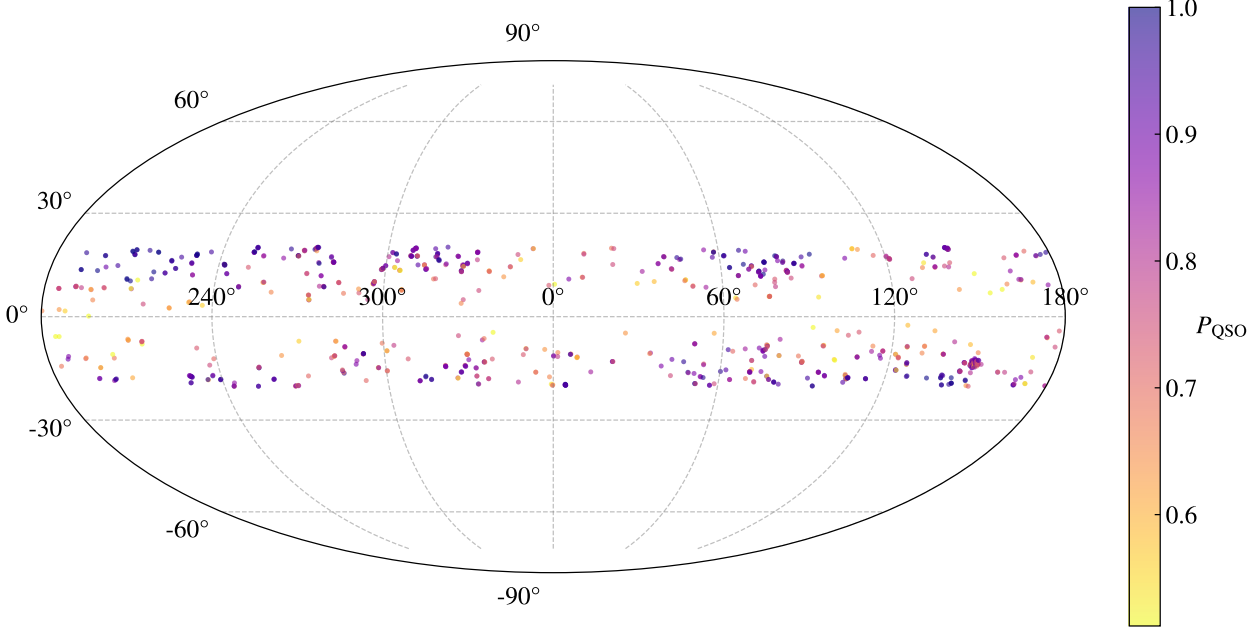


Figure 5. Spatial distribution of GPQ candidates ($|b| < 20^\circ$) in Galactic coordinates (Mollweide projection). Points are color-coded by the RF-derived quasar membership probability, P_{QSO} (color bar).

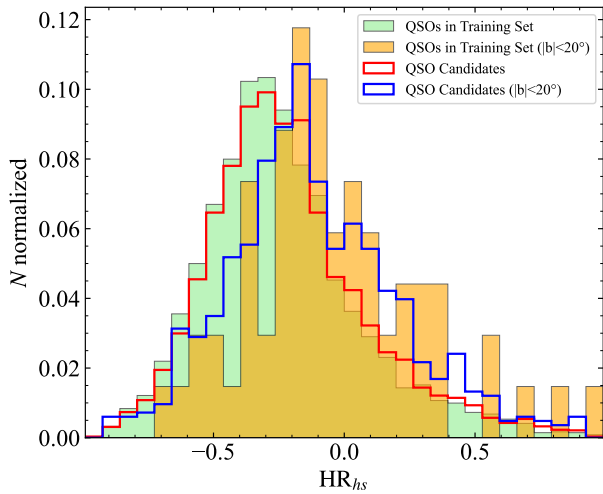


Figure 6. Normalized histograms of the HR_{hs} (hard – soft energy band hardness ratio, see table 3) for quasars. Filled histograms representing all-sky/galactic plane ($|b| < 20^\circ$) training set samples, and step outlines for selected all-sky/galactic plane candidates.

sources. To further suppress stellar contamination, we apply a probabilistic zero–proper-motion criterion based on *Gaia* astrometry. In addition, we estimate photometric redshifts for the quasar candidates using a RF–based regression model incorporating optical, infrared, and X-ray features.

Applying this framework to previously unclassified CSC sources, we identify a total of 6286 quasar candidates across the sky. Among these, 863 sources are located behind the Galactic plane ($|b| < 20^\circ$) and are identified as GPQ candidates, with 514 classified as high-confidence candidates based on their quasar membership probabilities. Pilot optical spectroscopy confirms two high-confidence GPQ candidates, 2CXO J031404.4+403900 ($z = 1.2582$) and 2CXO J031712.7+405301 ($z = 1.1313$), providing direct validation of our selection approach. Motivated by these initial confirmations, we will carry out more extensive spectroscopic follow-up of the full GPQ candidate sample.

The GPQ candidates exhibit systematically harder X-ray spectra than their high-latitude counterparts, a trend that is consistently observed in both the training sample and the newly identified candidates. This behavior is naturally explained by strong Galactic absorption along low-latitude sightlines, which preferentially attenuates soft X-ray photons. In addition, the GPQ candidates are systematically fainter in the optical, infrared, and X-ray bands compared with spectroscopically confirmed quasars, indicating that this work probes a population of faint or heavily obscured quasars that is largely inaccessible to purely optical or infrared selection methods.

Comparison with the unified all-sky quasar candidate catalog CatGlobe shows that while the majority of our

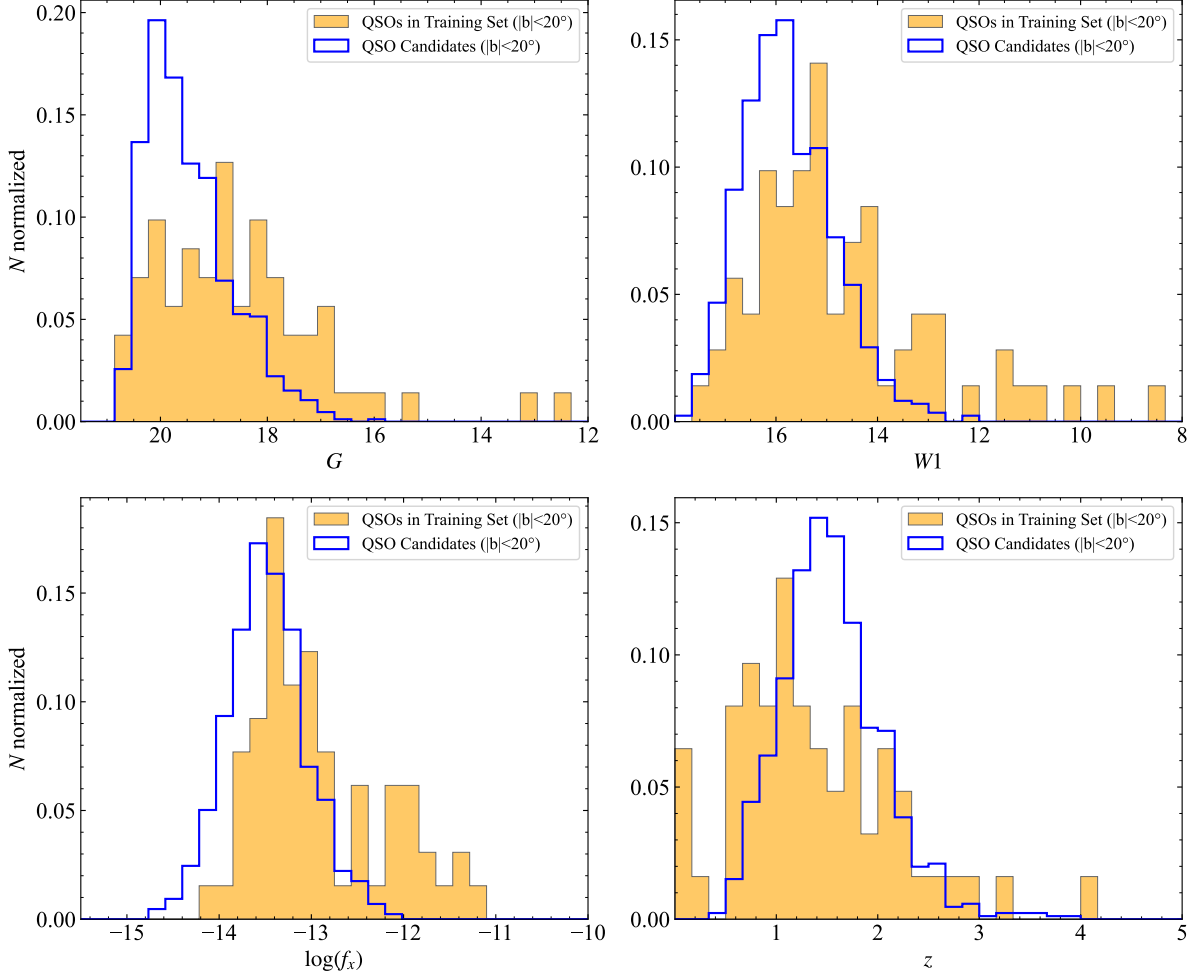


Figure 7. Normalized histograms of G , $W1$, $\log(f_x)$ (logarithm of X-ray flux in 0.5-7keV) and redshift (here, the redshifts of the QSO candidates are estimated photometrically via RF.) for GPQs and GPQ candidates. Filled histograms representing training set samples, and step outlines for selected candidates.

GPQ candidates have counterparts in existing catalogs, a significant fraction does not. These additional candidates exhibit properties consistent with the broader GPQ population, underscoring the importance of incorporating X-ray information to achieve a more complete census of quasars in the Galactic plane.

Overall, this study demonstrates that X-ray-based selection with *Chandra*, combined with multi-wavelength data and modern classification techniques, provides an effective pathway for identifying quasars in the most heavily obscured regions of the sky. The resulting GPQ candidate sample represents a valuable resource for future spectroscopic follow-up, for improving the uniformity of all-sky quasar catalogs, and for applications ranging from Galactic absorption studies to the construction of astrometric reference frames in the Galactic disk. Future extensions of this work to larger X-ray datasets and upcoming facilities will further enhance our

ability to uncover quasars hidden behind the Milky Way. The significant increase of GPQ sample will help improve the reference frame for astrometry by using GPQs as background references and probe the Milky Way interstellar and circumgalactic media with the absorption features of GPQs.

ACKNOWLEDGMENTS

We acknowledge the supports from National Natural Science Foundation of China under grant Nos. 12133001 and 12573110, as well as from National Key R&D Program of China (2025YFA1614101). We acknowledge the support of Shenzhen Science and Technology program (JCYJ20230807113910021) and the Natural Science Foundation of Top Talent of SZTU (GDRC202208).

This research made use of data from the *Chandra* X-ray Observatory, in particular the Chandra Source

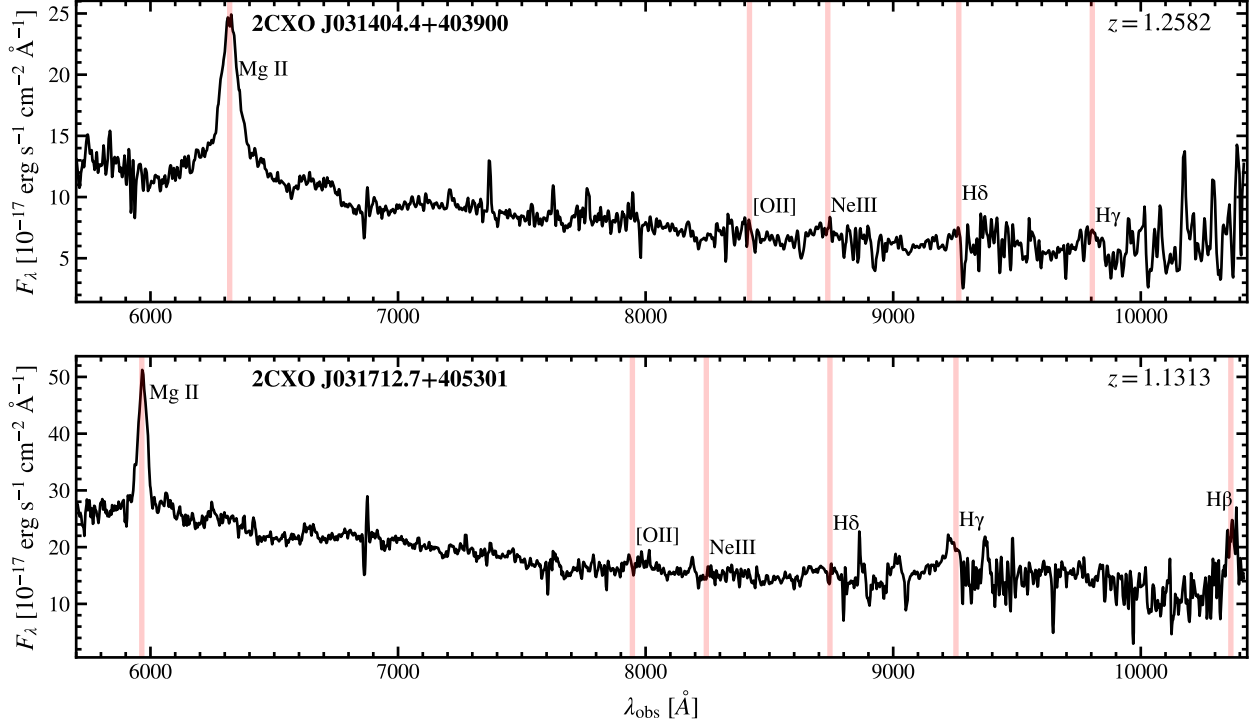


Figure 8. Spectra of the two identified GPQs from our pilot follow-up program with NGPS of Hale Telescope. We show flux- and wavelength-calibrated one-dimensional optical spectra of 2CXO J031404.4+403900 (upper) and 2CXO J031712.7+405301 (lower). The redshift inferred from identified emission lines is given in the upper-right corner of each panel. Strong emission features are labeled, and the spectra are displayed in the observed frame.

Catalog ([CSC website](#)) provided by the Chandra X-ray Center (CXC). It also made use of data from the European Space Agency (ESA) mission *Gaia* ([Gaia website](#)), processed by the *Gaia* Data Processing and Analysis Consortium ([DPAC consortium](#)). We used mid-infrared photometry from WISE/NEOWISE via the CatWISE2020 catalog and made use of the NASA/IPAC Infrared Science Archive (IRSA), which is funded by NASA and operated by the California Institute of Technology. Optical photometry was taken from the Pan-STARRS1 Surveys ([PS1](#)) and, where PS1 coverage is unavailable, from the NOIRLab Source Catalog DR2 ([NSC website](#)). We used dust reddening information based on *Planck*. We made use of public spectroscopic classifications from DESI DR1, SDSS DR18, and LAMOST; LAMOST is a National Major Scientific Project built by the Chinese Academy of Sciences, funded by the National Development and Reform Commission, and operated and managed by the National Astronomical Observatories, Chinese Academy of Sciences. This research

has made use of the SIMBAD database, operated at CDS, Strasbourg, France, and services provided by Astro Data Lab, part of the Community Science and Data Center Program of NSF NOIRLab, operated by AURA under a cooperative agreement with the U.S. National Science Foundation.

Spectroscopic observations were obtained with the Palomar 200-inch Hale Telescope at Palomar Observatory using the Next Generation Palomar Spectrograph ([NGPS](#)). We thank the Palomar Observatory staff for their support during the observations.

For DESI and SDSS, we acknowledge the respective collaborations and data release teams, their funding sources, and the observatory sites. In particular, we recognize the cultural significance of I'oligam Du'ag (Kitt Peak) to the Tohono O'odham Nation.

This work made use of TOPCAT and [scikit-learn](#) for catalog cross-matching and machine-learning analyses, and PYPEIT for spectroscopic data reduction.

REFERENCES

Ai, Y. L., Wu, X.-B., Yang, J., et al. 2016, AJ, 151, 24, doi: [10.3847/0004-6256/151/2/24](https://doi.org/10.3847/0004-6256/151/2/24)

Almeida, A., Anderson, S. F., Argudo-Fernández, M., et al. 2023, ApJS, 267, 44, doi: [10.3847/1538-4365/acda98](https://doi.org/10.3847/1538-4365/acda98)

- Bañados, E., Venemans, B. P., Mazzucchelli, C., et al. 2018, *Nature*, 553, 473, doi: [10.1038/nature25180](https://doi.org/10.1038/nature25180)
- Bao, T., Ponti, G., Haberl, F., et al. 2025, *A&A*, 704, A107, doi: [10.1051/0004-6361/202556747](https://doi.org/10.1051/0004-6361/202556747)
- Blanton, M. R., Bershady, M. A., Abolfathi, B., et al. 2017, *AJ*, 154, 28, doi: [10.3847/1538-3881/aa7567](https://doi.org/10.3847/1538-3881/aa7567)
- Breiman, L. 2001, *Mach. Learn.*, 45, 5, doi: [10.1023/A:1010933404324](https://doi.org/10.1023/A:1010933404324)
- Carrasco, D., Barrientos, L. F., Pichara, K., et al. 2015, *A&A*, 584, A44, doi: [10.1051/0004-6361/201525752](https://doi.org/10.1051/0004-6361/201525752)
- Chambers, K. C., Magnier, E. A., Metcalfe, N., et al. 2016, arXiv e-prints, arXiv:1612.05560, doi: [10.48550/arXiv.1612.05560](https://doi.org/10.48550/arXiv.1612.05560)
- Croom, S. M., Smith, R. J., Boyle, B. J., et al. 2004, *MNRAS*, 349, 1397, doi: [10.1111/j.1365-2966.2004.07619.x](https://doi.org/10.1111/j.1365-2966.2004.07619.x)
- Croom, S. M., Richards, G. T., Shanks, T., et al. 2009, *MNRAS*, 399, 1755, doi: [10.1111/j.1365-2966.2009.15398.x](https://doi.org/10.1111/j.1365-2966.2009.15398.x)
- Cui, X.-Q., Zhao, Y.-H., Chu, Y.-Q., et al. 2012, *RAA*, 12, 1197, doi: [10.1088/1674-4527/12/9/003](https://doi.org/10.1088/1674-4527/12/9/003)
- Cutri, R. M., Wright, E. L., Conrow, T., et al. 2013, Explanatory Supplement to the AllWISE Data Release Products., Explanatory Supplement to the AllWISE Data Release Products, by R. M. Cutri et al.
- Dawson, K. S., Schlegel, D. J., Ahn, C. P., et al. 2013, *AJ*, 145, 10, doi: [10.1088/0004-6256/145/1/10](https://doi.org/10.1088/0004-6256/145/1/10)
- Delgado, A. J., Alfaro, E. J., & Yun, J. L. 2011, *A&A*, 531, A141, doi: [10.1051/0004-6361/201116491](https://doi.org/10.1051/0004-6361/201116491)
- DESI Collaboration, Abdul-Karim, M., Adame, A. G., et al. 2025, arXiv e-prints, arXiv:2503.14745, doi: [10.48550/arXiv.2503.14745](https://doi.org/10.48550/arXiv.2503.14745)
- Di Matteo, T., Springel, V., & Hernquist, L. 2005, *Nature*, 433, 604, doi: [10.1038/nature03335](https://doi.org/10.1038/nature03335)
- Downes, R. A., Webbink, R. F., Shara, M. M., et al. 2001, *PASP*, 113, 764, doi: [10.1086/320802](https://doi.org/10.1086/320802)
- Eisenhardt, P. R. M., Marocco, F., Fowler, J. W., et al. 2020, *ApJS*, 247, 69, doi: [10.3847/1538-4365/ab7f2a](https://doi.org/10.3847/1538-4365/ab7f2a)
- Eisenstein, D. J., Zehavi, I., Hogg, D. W., et al. 2005, *ApJ*, 633, 560, doi: [10.1086/466512](https://doi.org/10.1086/466512)
- Evans, I. N., Evans, J. D., Martínez-Galarza, J. R., et al. 2024, *ApJS*, 274, 22, doi: [10.3847/1538-4365/ad6319](https://doi.org/10.3847/1538-4365/ad6319)
- Fan, X., Bañados, E., & Simcoe, R. A. 2023, *ARA&A*, 61, 373, doi: [10.1146/annurev-astro-052920-102455](https://doi.org/10.1146/annurev-astro-052920-102455)
- Flesch, E. W. 2023, *Open J. Astrophys*, 6, 49, doi: [10.21105/astro.2308.01505](https://doi.org/10.21105/astro.2308.01505)
- Fu, Y., Wu, X.-B., Yang, Q., et al. 2021, *ApJS*, 254, 6, doi: [10.3847/1538-4365/abe85e](https://doi.org/10.3847/1538-4365/abe85e)
- Fu, Y., Wu, X.-B., Jiang, L., et al. 2022, *ApJS*, 261, 32, doi: [10.3847/1538-4365/ac7f3e](https://doi.org/10.3847/1538-4365/ac7f3e)
- Fu, Y., Wu, X.-B., Li, Y., et al. 2024, *ApJS*, 271, 54, doi: [10.3847/1538-4365/ad2ae6](https://doi.org/10.3847/1538-4365/ad2ae6)
- Fu, Y., Wu, X.-B., Bouwens, R. J., et al. 2025, *ApJS*, 279, 54, doi: [10.3847/1538-4365/ade999](https://doi.org/10.3847/1538-4365/ade999)
- Gaia Collaboration, Mignard, F., Klioner, S. A., et al. 2018a, *A&A*, 616, A14, doi: [10.1051/0004-6361/201832916](https://doi.org/10.1051/0004-6361/201832916)
- Gaia Collaboration, Brown, A. G. A., Vallenari, A., et al. 2018b, *A&A*, 616, A1, doi: [10.1051/0004-6361/201833051](https://doi.org/10.1051/0004-6361/201833051)
- Gaia Collaboration, Klioner, S. A., Lindegren, L., et al. 2022, *A&A*, 667, A148, doi: [10.1051/0004-6361/202243483](https://doi.org/10.1051/0004-6361/202243483)
- Gaia Collaboration, Bailer-Jones, C. A. L., Teyssier, D., et al. 2023a, *A&A*, 674, A41, doi: [10.1051/0004-6361/202243232](https://doi.org/10.1051/0004-6361/202243232)
- Gaia Collaboration, Vallenari, A., Brown, A. G. A., et al. 2023b, *A&A*, 674, A1, doi: [10.1051/0004-6361/202243940](https://doi.org/10.1051/0004-6361/202243940)
- Giardino, G., Favata, F., Micela, G., Sciortino, S., & Winston, E. 2007, *A&A*, 463, 275, doi: [10.1051/0004-6361:20066424](https://doi.org/10.1051/0004-6361:20066424)
- Ho, T. K. 1995, in Proceedings of 3rd International Conference on Document Analysis and Recognition, Vol. 1, 278–282 vol.1, doi: [10.1109/ICDAR.1995.598994](https://doi.org/10.1109/ICDAR.1995.598994)
- Humphrey, P. J., & Buote, D. A. 2008, *ApJ*, 689, 983, doi: [10.1086/592590](https://doi.org/10.1086/592590)
- Huo, Z.-Y., Fu, Y., Huang, Y., et al. 2025, *ApJS*, 278, 6, doi: [10.3847/1538-4365/adba52](https://doi.org/10.3847/1538-4365/adba52)
- Im, M., Lee, I., Cho, Y., et al. 2007, *ApJ*, 664, 64, doi: [10.1086/518734](https://doi.org/10.1086/518734)
- Inayoshi, K., Visbal, E., & Haiman, Z. 2020, *ARA&A*, 58, 27, doi: [10.1146/annurev-astro-120419-014455](https://doi.org/10.1146/annurev-astro-120419-014455)
- Jiang, H., Hu, Z., Xu, M., et al. 2018, in Society of Photo-Optical Instrumentation Engineers (SPIE) Conference Series, Vol. 10702, Ground-based and Airborne Instrumentation for Astronomy VII, ed. C. J. Evans, L. Simard, & H. Takami, 107022L, doi: [10.1117/12.2312550](https://doi.org/10.1117/12.2312550)
- Jin, J.-J., Wu, X.-B., Fu, Y., et al. 2023, *ApJS*, 265, 25, doi: [10.3847/1538-4365/acaf89](https://doi.org/10.3847/1538-4365/acaf89)
- Jönsson, H., Holtzman, J. A., Allende Prieto, C., et al. 2020, *AJ*, 160, 120, doi: [10.3847/1538-3881/aba592](https://doi.org/10.3847/1538-3881/aba592)
- Kormendy, J., & Ho, L. C. 2013, *ARA&A*, 51, 511, doi: [10.1146/annurev-astro-082708-101811](https://doi.org/10.1146/annurev-astro-082708-101811)
- Kundu, A., Maccarone, T. J., & Zepf, S. E. 2007, *ApJ*, 662, 525, doi: [10.1086/518021](https://doi.org/10.1086/518021)
- Liu, C., Côté, P., Peng, E. W., et al. 2020, *ApJS*, 250, 17, doi: [10.3847/1538-4365/abad91](https://doi.org/10.3847/1538-4365/abad91)
- Liu, Q. Z., van Paradijs, J., & van den Heuvel, E. P. J. 2006, *A&A*, 455, 1165, doi: [10.1051/0004-6361:20064987](https://doi.org/10.1051/0004-6361:20064987)

- Liu, Q. Z., van Paradijs, J., & van den Heuvel, E. P. J. 2007, *A&A*, 469, 807, doi: [10.1051/0004-6361:20077303](https://doi.org/10.1051/0004-6361:20077303)
- Luo, A.-L., Zhao, Y.-H., Zhao, G., et al. 2015, *RAA*, 15, 1095, doi: [10.1088/1674-4527/15/8/002](https://doi.org/10.1088/1674-4527/15/8/002)
- Lyke, B. W., Higley, A. N., McLane, J. N., et al. 2020, *ApJS*, 250, 8, doi: [10.3847/1538-4365/aba623](https://doi.org/10.3847/1538-4365/aba623)
- Lyu, B., Wu, X.-B., Jin, J.-J., et al. 2025, arXiv e-prints, arXiv:2512.02836, doi: [10.48550/arXiv.2512.02836](https://doi.org/10.48550/arXiv.2512.02836)
- Ma, C., Arias, E. F., Bianco, G., et al. 2009, *IERS Technical Note*, 35, 1
- Megeath, S. T., Gutermuth, R., Muzerolle, J., et al. 2012, *AJ*, 144, 192, doi: [10.1088/0004-6256/144/6/192](https://doi.org/10.1088/0004-6256/144/6/192)
- Mineo, S., Gilfanov, M., & Sunyaev, R. 2012, *MNRAS*, 419, 2095, doi: [10.1111/j.1365-2966.2011.19862.x](https://doi.org/10.1111/j.1365-2966.2011.19862.x)
- Nidever, D. L., Dey, A., Fasbender, K., et al. 2021, *AJ*, 161, 192, doi: [10.3847/1538-3881/abd6e1](https://doi.org/10.3847/1538-3881/abd6e1)
- Ozawa, H., Grosso, N., & Montmerle, T. 2005, *A&A*, 429, 963, doi: [10.1051/0004-6361:20040480](https://doi.org/10.1051/0004-6361:20040480)
- Pâris, I., Petitjean, P., Ross, N. P., et al. 2017, *A&A*, 597, A79, doi: [10.1051/0004-6361/201527999](https://doi.org/10.1051/0004-6361/201527999)
- Pedregosa, F., Varoquaux, G., Gramfort, A., et al. 2011, *J. Mach. Learn. Res.*, 12, 2825
- Planck Collaboration, Aghanim, N., Ashdown, M., et al. 2016, *A&A*, 596, A109, doi: [10.1051/0004-6361/201629022](https://doi.org/10.1051/0004-6361/201629022)
- Povich, M. S., Smith, N., Majewski, S. R., et al. 2011, *ApJS*, 194, 14, doi: [10.1088/0067-0049/194/1/14](https://doi.org/10.1088/0067-0049/194/1/14)
- Prochaska, J., Hennawi, J., Westfall, K., et al. 2020, *The Journal of Open Source Software*, 5, 2308, doi: [10.21105/joss.02308](https://doi.org/10.21105/joss.02308)
- Rebull, L. M., Koenig, X. P., Padgett, D. L., et al. 2011, *ApJS*, 196, 4, doi: [10.1088/0067-0049/196/1/4](https://doi.org/10.1088/0067-0049/196/1/4)
- Richards, G. T., Fan, X., Newberg, H. J., et al. 2002, *AJ*, 123, 2945, doi: [10.1086/340187](https://doi.org/10.1086/340187)
- Richter, P. 2006, *Reviews in Modern Astronomy*, 19, 31, doi: [10.1002/9783527619030.ch2](https://doi.org/10.1002/9783527619030.ch2)
- Riello, M., De Angeli, F., Evans, D. W., et al. 2021, *A&A*, 649, A3, doi: [10.1051/0004-6361/202039587](https://doi.org/10.1051/0004-6361/202039587)
- Ritter, H., & Kolb, U. 2015, *Acta Polytech. CTU Proc.*, 2, 21, doi: [10.14311/APP.2015.02.0021](https://doi.org/10.14311/APP.2015.02.0021)
- Ross, N. P., Myers, A. D., Sheldon, E. S., et al. 2012, *ApJS*, 199, 3, doi: [10.1088/0067-0049/199/1/3](https://doi.org/10.1088/0067-0049/199/1/3)
- Savage, B. D., & Sembach, K. R. 1996, *ARA&A*, 34, 279, doi: [10.1146/annurev.astro.34.1.279](https://doi.org/10.1146/annurev.astro.34.1.279)
- Sazonov, S., & Khabibullin, I. 2017, *MNRAS*, 466, 1019, doi: [10.1093/mnras/stw3113](https://doi.org/10.1093/mnras/stw3113)
- Sazonov, S., Paizis, A., Bazzano, A., et al. 2020, *NewAR*, 88, 101536, doi: [10.1016/j.newar.2020.101536](https://doi.org/10.1016/j.newar.2020.101536)
- Schlegel, D. J., Finkbeiner, D. P., & Davis, M. 1998, *ApJ*, 500, 525, doi: [10.1086/305772](https://doi.org/10.1086/305772)
- Schneider, D. P., Richards, G. T., Hall, P. B., et al. 2010, *AJ*, 139, 2360, doi: [10.1088/0004-6256/139/6/2360](https://doi.org/10.1088/0004-6256/139/6/2360)
- Soria, R., & Kong, A. K. H. 2002, *ApJL*, 572, L33, doi: [10.1086/341445](https://doi.org/10.1086/341445)
- Taylor, M. B. 2005, in *Astronomical Society of the Pacific Conference Series*, Vol. 347, *Astronomical Data Analysis Software and Systems XIV*, ed. P. Shopbell, M. Britton, & R. Ebert, 29
- van der Hucht, K. A. 2001, *NewAR*, 45, 135, doi: [10.1016/S1387-6473\(00\)00112-3](https://doi.org/10.1016/S1387-6473(00)00112-3)
- van der Hucht, K. A. 2006, *A&A*, 458, 453, doi: [10.1051/0004-6361:20065819](https://doi.org/10.1051/0004-6361:20065819)
- Walter, R., Lutovinov, A. A., Bozzo, E., & Tsygankov, S. S. 2015, *A&A Rv*, 23, 2, doi: [10.1007/s00159-015-0082-6](https://doi.org/10.1007/s00159-015-0082-6)
- Wang, H., Ai, Y., Zhang, Y., et al. 2025, *ApJ*, 985, 23, doi: [10.3847/1538-4357/adc7b8](https://doi.org/10.3847/1538-4357/adc7b8)
- Wenger, M., Ochsenbein, F., Egret, D., et al. 2000, *A&AS*, 143, 9–22, doi: [10.1051/aas:2000332](https://doi.org/10.1051/aas:2000332)
- Werk, J., Tchernyshyov, K., Bish, H., et al. 2024, *ApJS*, 273, 21, doi: [10.3847/1538-4365/ad58df](https://doi.org/10.3847/1538-4365/ad58df)
- Wright, E. L., Eisenhardt, P. R. M., Mainzer, A. K., et al. 2010, *AJ*, 140, 1868, doi: [10.1088/0004-6256/140/6/1868](https://doi.org/10.1088/0004-6256/140/6/1868)
- Wu, X.-B., Wang, F., Fan, X., et al. 2015, *Nature*, 518, 512, doi: [10.1038/nature14241](https://doi.org/10.1038/nature14241)
- York, D. G., Adelman, J., Anderson, Jr., J. E., et al. 2000, *AJ*, 120, 1579, doi: [10.1086/301513](https://doi.org/10.1086/301513)
- Zhang, Z., Gilfanov, M., Voss, R., et al. 2011, *A&A*, 533, A33, doi: [10.1051/0004-6361/201116936](https://doi.org/10.1051/0004-6361/201116936)